RSC Advances

PAPER

View Article Online
View Journal | View Issue

Cite this: *RSC Adv.*, 2025, **15**, 28889

A dual-type I/II NIR photosensitizer for effective cancer photodynamic therapy with enhanced ROS generation

Shuhua Cao,[a] Yuchang Liu,[a] Xishi Tai,[a] Li Shen,[a] Hekai Yang,[b] Fahui Li,[b] Binglin Sui,[a] Pengju Ma,[a] Lingxuan Zhu,[a] Bin Gao,[a] Anlin Wang*[c] and Mohammad Azam[d]

Received 21st July 2025
Accepted 28th July 2025

DOI: 10.1039/d5ra05267j

rsc.li/rsc-advances

Based on the cyanine dye scaffold, two photosensitizers (PSs) (C1 and C2) were successfully synthesized. These PSs exhibited a maximum absorption wavelength of 660 nm, falling within the near-infrared window. Compared to the commercially available photosensitizer ICG, the newly developed PSs demonstrated enhanced reactive oxygen species (ROS) generation under lower light doses. Notably, these PSs can simultaneously produce both singlet oxygen ($^1O_2$) and superoxide anion radicals ($O_2^{\bullet-}$), classifying them as dual type I/II PSs. Compared with C1, the $^1O_2$ quantum yield of C2 was higher, as high as 10.6 times that of ICG. Theoretical calculations revealed that the molecules of C2 possessed a small singlet–triplet energy gap (ΔE_{S-T}), which facilitated more efficient intersystem crossing (ISC) from the singlet to triplet state, thereby promoting greater ROS generation. Experiments showed that C1 and C2 were located in mitochondria and could cause a decrease in mitochondrial membrane potential, leading to cell death. Animal experiments have shown that C2 effectively suppressed tumor growth without side effects.

Introduction

In recent years, the incidence of cancer has remained high and has become a threat to human health.[1] Traditional surgical treatment, chemotherapy and radiation therapy all have side effects on the human body. In order to avoid side effects during the treatment of tumors, the treatment strategy of oxidative stress is receiving increasing attention.[2–6] Among them, photodynamic therapy (PDT) has garnered increasing attention due to its spatiotemporal controllability and absence of side effects.[5,7]

PDT involves the generation of reactive oxygen species (ROS) at the tumor site through electron transfer or energy transfer mediated by PSs upon light irradiation, thereby inducing tumor cell death.[7–9] Consequently, the yield of ROS critically influences the therapeutic efficacy of PDT. PSs for PDT can be classified into two types. Type I PSs do not require oxygen participation and generate superoxide radicals ($O_2^{\bullet-}$) *via* electron transfer, whereas type II PSs rely on oxygen and convert surrounding oxygen into singlet oxygen ($^1O_2$) through energy transfer.[7,10] Currently, the majority of PSs belong to type II, whose therapeutic efficacy is significantly limited by hypoxia in the solid tumor interior.[10,11] However, the therapeutic efficacy of type-I PDT alone is fundamentally constrained by two limitations: the attenuation of light penetration in tissues and the inherently short diffusion radius of ROS species (~100 nm), which collectively lead to incomplete tumor eradication and subsequent recurrence.[12,13] Moreover, solid tumors consistently exhibit a transition from the normoxic microenvironment surrounding proliferation to a gradually hypoxic state within the central core.[14] Therefore, developing PSs capable of producing ROS under both oxygen-rich (aerobic) and hypoxic (oxygen-deficient) conditions is of great significance for enhancing tumor therapeutic efficacy. At present, most of these dual type I/II photosensitizers are aggregation induced emission (AIE) photosensitizers,[15,16] and there are relatively few applications of cyanine dyes in this field.

Moreover, the production of ROS in PSs used for PDT affects the therapeutic effect. To generate more ROS, heavy atom iodine was introduced into the PSs molecule. Iodine, as an essential trace element for the human body, can increase the spin–orbit coupling after introducing PSs molecules to improve the ISC efficiency, and then produce more ROS.[17,18] Up to now, many studies have increased the production of ROS by introducing heavy atoms into photosensitizer molecules.[18–21] But most of them can only produce one type of reactive oxygen species instead of dual types I/II.

[a]*College of Chemistry, Chemical and Environmental Engineering, Weifang University, No. 5147 Dongfeng Street, Weifang, 261061, P. R. China*

[b]*School of Pharmacy, Shandong Second Medical University, No. 7166 Baotong Street, Weifang, 261053, P. R. China*

[c]*Affiliated Beijing Chaoyang Hospital, Capital Medical University, No. 8 Gongren Tiyuchang Nanlu, Chaoyang District, Beijing, 100020, P. R. China. E-mail: jordan0309@126.com*

[d]*Department of Chemistry, College of Science, King Saud University, PO Box 2455, Riyadh 11451, Saudi Arabia*

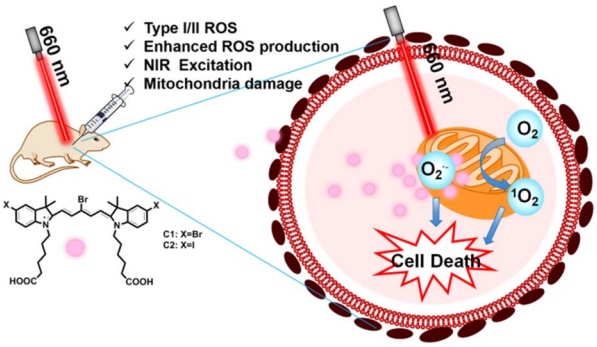

Scheme 1 Chemical structure of photosensitizer and schematic diagram of PDT process.

Further more, near infrared light has a deeper penetration depth and is harmless to the human body, attracting increasing attention. Therefore, developing near-infrared PSs can effectively penetrate tissues and treat solid tumors.[22–26] At present, the most commonly used PSs in clinical is still Photofrin, which was the first PS to receive FDA approval.[27] Nevertheless, its PDT efficiency is hampered by the low absorption intensity during the near infrared region.[28] Currently, most PSs exert photodynamic effects within the cytoplasm of tumor cells.[29–31] However, the low oxygen content in the cytoplasm of tumor cells leads to poor photodynamic effects. Cyanine dyes contain a positive charge, making them easy to enter the mitochondria of tumor cells, which is the site for aerobic respiration in cells with high oxygen content. Moreover, the structure of cyanine dyes is easily regulated, making their absorption wavelength in the near-infrared region.

Herein, we have successfully synthesized two pentamethine cyanine dye molecules as PSs for PDT of tumors. Theoretical calculations have found that the PSs molecules can effectively reduce singlet–triplet energy difference (ΔE_{S-T}), which make it easier for PSs molecules to ISC from excited singlet state to triplet state. It is widely known that PSs molecules can only convert molecular oxygen into ROS when they are in the triplet state. More notably, these PSs molecule can not only generate $^1O_2$ *via* the type II mechanism but also produce $O_2^{\cdot-}$ through the type I pathway. This dual functionality holds significant importance for enhancing the therapeutic efficacy of PDT. In order to improve its water solubility, a carboxyl group was introduced into the indole nitrogen of the indole ring. The maximum absorption wavelength of these PSs was about 660 nm. As shown in the Scheme 1, These PSs had advantages such as being in the near-infrared treatment window, high ROS generation, good photodynamic performance, and low dark toxicity.

Results and discussion

Synthesis of PSs

As shown in Scheme S1, the synthesis route of PSs included three parts: the synthesis of condensing agents, quaternary ammonium salts, and the final product PSs. A condensing agent was synthesized by reacting 2,3-dibromo-4-oxobut-2-enoic acid with aniline. Indole was synthesized using 4-iodophenylhydrazine hydrochloride as raw material, and then reacted with 6-bromohexanoic acid to generate quaternary ammonium salt. Finally, the quaternary ammonium salt was reacted with a condensing agent to obtain a PS. The products were characterized by high-resolution mass spectrometry (HRMS) and nuclear magnetic resonance. The results are shown in Fig. S4–S18.

Photophysical properties and photostability

The wavelength of the excitation light used in photodynamic therapy should preferably be the maximum absorption wavelength of the PS, which can ensure that the PSs absorb more energy. The absorption and fluorescence spectra of PS C1 and C2 are shown in Fig. S1. From Fig. S1, it can be seen that the maximum absorption wavelengths of C1 and C2 were 650 nm and 660 nm, respectively. The maximum absorption wavelengths of C1 and C2 were both located in the near-infrared region, indicating that these PSs were beneficial for photodynamic therapy. PSs are prone to degradation under excitation light irradiation, therefore the photostability of PSs can affect their photodynamic performance. In order to study the photostability of PSs, the degradation of PSs at different energies was measured using absorption spectroscopy. As shown in Fig. 1a–c the photostability of PSs C1, C2, and commercial ICG. After being illuminated with 162 J cm^{-2} energy, the absorption intensities of C1, C2, and ICG changed to the original 73%, 53% and 15%, respectively. These results indicated that the photostability of C1 and C2 was much better than that of ICG.

ROS testing

In order to determine the photodynamic properties of PSs C1 and C2, their ability to generate ROS in solution was tested separately. The maximum absorption wavelength of 1,3-diphenylisobenzofuran (DPBF) is around 415 nm. The absorption of DPBF will decrease when $^1O_2$ is generated. C1 and C2 was mixed with DPBF in the dichloromethane. The mixture was

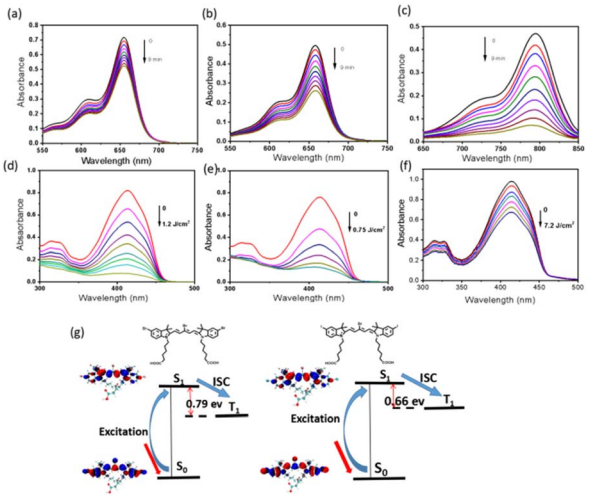

Fig. 1 The photostability of C1 (a), C2 (b) and ICG (c), absorbance decreased of DPBF (415 nm) with increasing the light dose (660 nm, 30 mW cm^{-2}) in the presence of C1 (d), C2 (e) and ICG (f). (g) HOMO–LUMO distribution and singlet–triplet energy difference of C1 and C2.

irradiated with 660 nm light (30 mW cm^{-2}) for a certain period of time, then the absorption of the DPBF was measured. The experimental results indicated that both C1 and C2 can reduce the absorption of DPBF by more than 90% under the illumination of 1.2 J cm^{-2} and 0.75 J cm^{-2}, respectively, indicating the C1 and C2 generated a large amount of $^1O_2$ in the solution (Fig. 1d and e). Compared to ICG (Fig. 1f), C1 and C2 produce more $^1O_2$ at lower light doses. Under the irradiation of the same energy of light, C2 had a better ability to produce $^1O_2$ than C1. We calculated the $^1O_2$ quantum yields of C1 and C2 to be 2.8 and 7.4, respectively, based on ICG ($^1O_2$ quantum yield of 0.7). The $^1O_2$ quantum yield of C2 was higher than that of photosensitizers with similar structures (Cy5, Ph-Cy5, XAN-Cy5, AN-Cy5), and was approximately the same as that of ANPh-Cy5, but lower than the PSs containing heavy atoms (I-Cy5) in the reference literature.[32]

In order to further reveal the mechanism of photodynamic therapy, Singlet Oxygen Sensor Green® (SOSG) and dihydrorhodamine 123 (DHR123) were used as fluorescent probes for the generation of $^1O_2$ and $O_2^{\bullet-}$ during light irradiation, respectively. As shown in Fig. 2a and b, the mixture of PS C1 and SOSG showed a significant increase in fluorescence intensity under illumination, indicating that C1 can produce a large amount of $^1O_2$ under illumination. Under the same conditions, C2 can also enhance the fluorescence of SOSG, and the fluorescence intensity was much higher than that of C1, indicating that C2 can also produce $^1O_2$ under light conditions, the amount of $^1O_2$ was much more than that of C1. These results are consistent with those measured by DPBF. From Fig. 2c and d, the mixture of C1 and DHR123 showed stronger fluorescence intensity with increasing illumination time, indicating that C1 can generate $O_2^{\bullet-}$ under illumination. Under the same conditions, C2 can produce less fluorescence, indicating that C2 can produce less $O_2^{\bullet-}$. These results indicated that C1 and C2 produced both $^1O_2$ and $O_2^{\bullet-}$ simultaneously, belonging to type I & II photosensitizers. Moreover, C2, which produced more $^1O_2$, produced slightly fewer $O_2^{\bullet-}$. These results could also explain why the $^1O_2$ quantum yield of C2 was lower than that of PSs containing I with similar structures (I-Cy5) in the reference literature,[32] possibly because it generated $O_2^{\bullet-}$ while generating $^1O_2$, and there is competition between the two ROS.[34]

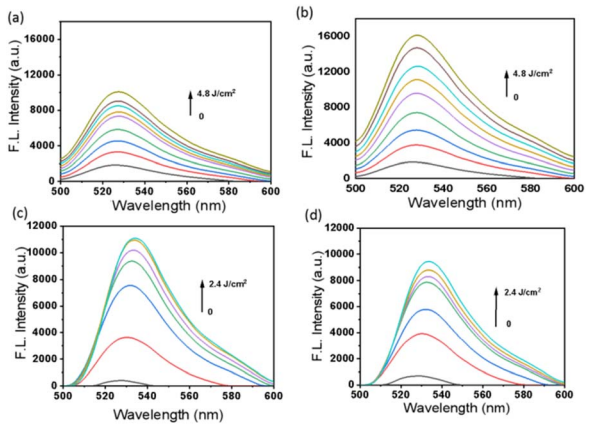

Fig. 2 Fluorescence spectra changes of Singlet Oxygen Sensor Green (SOSG) for $^1O_2$ detection. (a) C1 (10 μM), SOSG (5 μM), (b) C2 (10 μM); SOSG (5 μM); fluorescence spectra changes of DHR123 for $O_2^{\bullet-}$ detection. (c) C1 (10 μM), DHR123 (60 μM), (d) C2 (10 μM), DHR123 (60 μM).

Theoretical calculations

To study the mechanism of PSs molecules to produce ROS, we used density functional calculations to determine the highest occupied molecular orbital-lowest unoccupied molecular orbital (HOMO–LUMO) energy gap (E_{gap}) and the singlet–triplet energy difference (ΔE_{S-T}) of the PSs molecules. Ground state optimization was performed using the B3LYP functional with the def2-TZVP basis set. The vertical excitation energies were calculated using the BLYP functional of TD-TDFT with the def2-TZVP basis set. As shown in Fig. 1g, the distribution of electron clouds on the HOMO of C1 and C2 was characterized by extending along the entire conjugate main chain. While the cloud of electrons in the LUMO was mainly concentrated in the C1 and C2 receptor sites. The E_{gap} of C1 was slightly higher than that of C2, which was consistent with the redshift of the maximum absorption wavelength of C2. Due to the heavy atom effect, C2 molecules have a narrower ΔE_{S-T}, which can promote ISC and generate more ROS.[33] This result is consistent with the ROS results obtained through DPBF testing.

Organelle localization

Type II PDT requires the participation of oxygen to produce ROS. Mitochondria are the places where cells undergo aerobic respiration and contain abundant oxygen. Therefore, PSs targeting mitochondria will be beneficial for PDT. To determine the localization of PSs molecules in organelles, we performed colocalization experiments using the Lyso Tracker Red, Mito Tracker Green, and Hoechst 33342 commercial dyes to stain cells and locate lysosomes, mitochondria, and nuclear organelles, respectively. As shown in Fig. 3, the staining sites of C1 and C2 almost overlap with the Mito Tracker mitochondrial probe, with Pearson coefficients of 0.916 and 0.911, respectively. However, there was only a slight overlap in the staining of C1 and C2 with lysosomal and nuclear probes, with Pearson coefficients around 0.6 and 0.4, indicating that C1 and C2 were localized in mitochondria. Mitochondria, as the site of aerobic respiration, have a rich oxygen content, which is more conducive to PDT.

Intracellular ROS production

To further determine the potential of PSs C1 and C2 for *in vivo* use, intracellular ROS production was measured. The DCFH-DA probe was used to measure the intracellular ROS. The DCFH-DA probe without fluorescence can penetrate the cell membrane and enter the cell. Under the hydrolysis of intracellular esterase, DCFH-DA is converted into DCFH that cannot penetrate the cell membrane, thus the probe is loaded into the cell. The non fluorescent DCFH transforms into green fluorescent DCF under the action of intracellular ROS, and its fluorescence intensity reflects the level of intracellular ROS. As shown in Fig. 4,

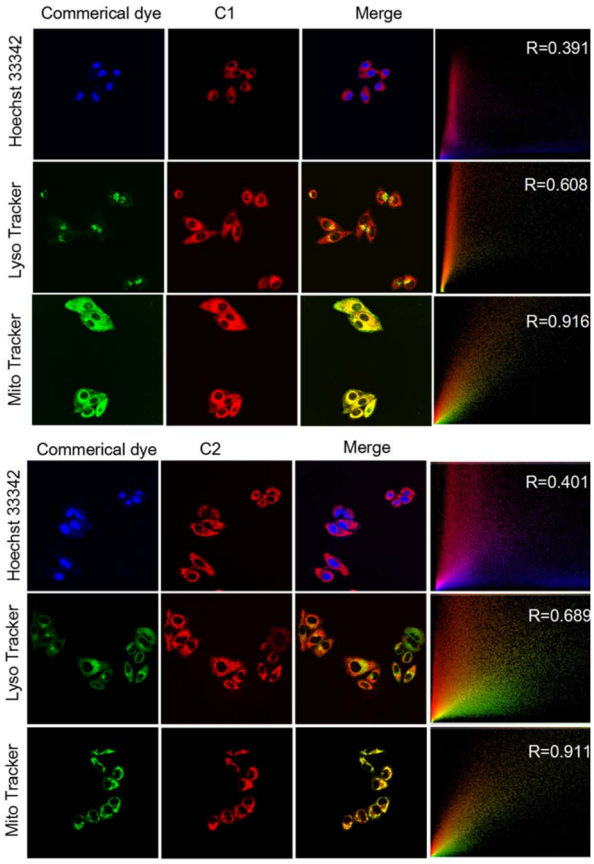

Fig. 3 Subcellular localization for C1 and C2 in living HepG2 cells with laser confocal scanning microscopy.

intracellular ROS experimental results showed that C1 and C2 could produce bright green fluorescence inside the cell under 660 nm light irradiation (30 mW cm^{-2}), while the control group did not have fluorescence, indicating that C1 and C2 can produce a large amount of ROS inside the cell with 660 nm light irradiation. These results are consistent with the ROS test results in the solution.

Mitochondrial damage

Considering that C1 and C2 were localized in mitochondria and could produce ROS, the mitochondrial membrane potential experiments were performed. JC-1 is a fluorescent probe used to detect mitochondrial membrane potential. When the mitochondrial membrane potential is high, JC-1 exists in the mitochondria as a red fluorescent polymer, while when the mitochondrial membrane potential is low, JC-1 exists in the mitochondria as a green fluorescent monomer. The decrease in mitochondrial membrane potential is a landmark event in the early stages of cell apoptosis. Therefore, the transition of JC-1 from red fluorescence to green fluorescence indicates cell membrane damage. After the cells took up the PSs, they were stained with JC-1 fluorescent probe and then illuminated. The changes in JC-1 fluorescence signal of the cells before and after PDT were observed under laser confocal microscopy, as shown in Fig. 5. The C1 and C2 groups were similar to the control group before light irradiation, with red fluorescence as the main fluorescence. After light irradiation, the red fluorescence disappeared and the green fluorescence increased in C1 and C2 groups. From the merge channel, it could be seen that green fluorescence was the main fluorescence, indicating that ROS generated by light irradiation in the presence of PSs C1 and C2 caused damage to mitochondria.

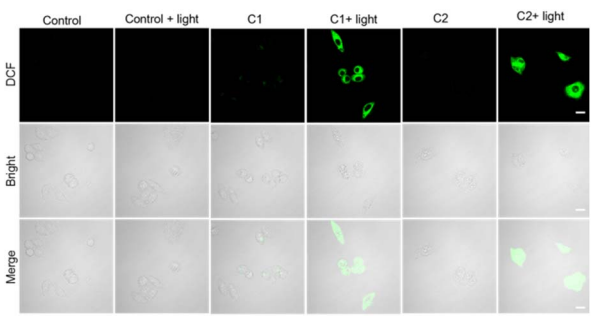

Fig. 4 Intracellular ROS in HepG2 cells after different treatments stained with DCFH-DA. Scale bars: 20 μm.

Cell viability

To measure the toxicity of PSs on tumor cells, calcein AM and PI were used to stain live and dead cells. Calcein AM without fluorescence easily penetrates the cell membrane and enters the cell. Under the action of endogenous esterase, it is hydrolyzed into calcein molecules that emit strong green fluorescence. Moreover, calcein cannot pass through the cell membrane and be retained within the cell, while dead cells lack esterase and cannot produce calcein with strong green fluorescence. However, PI cannot penetrate the cell membrane and can only stain dead cells with incomplete cell membranes. Therefore, using the calcein AM and PI dual staining kit, the fluorescence differences of live and dead cells can be observed very clearly. After being treated with PSs C1 and C2 and exposed to 660 nm light (30 mW cm^{-2}, 10 min), the cells were stained with calcein AM and PI, as shown in Fig. 6. There was no significant change in cell activity before and after light exposure in the control group. Under dark conditions, groups C1 and C2 exhibited

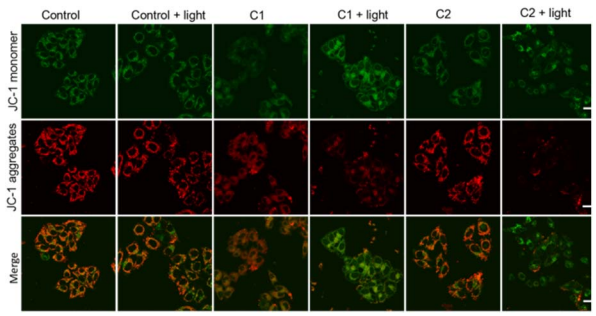

Fig. 5 Mitochondrial membrane potential assay for C1 and C2 mediated photodamage of mitochondria. Cells in C1 + light and C2 + light groups were irradiated with 660 nm LED light (18 J cm^{-2}). Scale bars: 20 μm.

a significant amount of green fluorescence, with almost no red fluorescence, indicating low dark toxicity of C1 and C2. After exposure to light, the green fluorescence disappeared and a large amount of red fluorescence appeared in groups C1 and C2, indicating a significant amount of cell death after exposure to PS light. The MTT method further confirmed the killing ability of C1 and C2 on cells. As shown in Fig. S2, C1 and C2 have strong killing ability against various cells such as HepG2 and 4T1.

Antitumor activity

The positive results of cell experiments inspired us to further conduct animal experiments. All procedures were in accordance with the Guide for the Care and Use of Laboratory Animal Resources and the National Research Council, and were approved by the Institutional Animal Care and Use Committee of Shandong Second Medical University. Approval ethics number: 2023SDL238. The *in situ* injection model of 4T1 tumor bearing mice was used to study the *in vivo* anti-tumor activity of PSs C1 and C2. C1 and C2 were injected into the tumor at a dose of 1 mg kg^{-1}. The mice were irradiated with 660 nm light (25 mW cm^{-2}, 20 min) after 3 hours at the tumor site. In addition, six groups of experiments were conducted, including: (1) injecting PBS only (PBS group), (2) injecting PBS and then lighting (PBS + light group), (3) injecting C1 only (C1 group), (4) injecting C1 and then lighting (C1 + light group), (5) injecting C2 only (C2 group), (6) injecting C2 and then lighting (C2 + light group). To monitor the growth status of mice, their body weight was measured every two days. As shown in Fig. 7a, the weight of each group of mice increased with time. The anti-tumor effect was evaluated by measuring the tumor volume of each group of mice for 14 days (Fig. 7b–d). The tumor volume in the PBS group and PBS light group increased by about 7 times and 7.5 times, respectively, indicating that near-infrared light irradiation did not have an inhibitory effect on tumors. In the absence of light, the tumor volume of both C1 and C2 groups increased by about 6 times, indicating that the PSs did not have the ability to inhibit tumor growth without excitation of light. Compared with the above six groups, the tumor volume in the C1 and C2 light groups was significantly inhibited, especially in the C2 light group where the tumor volume remained the same as

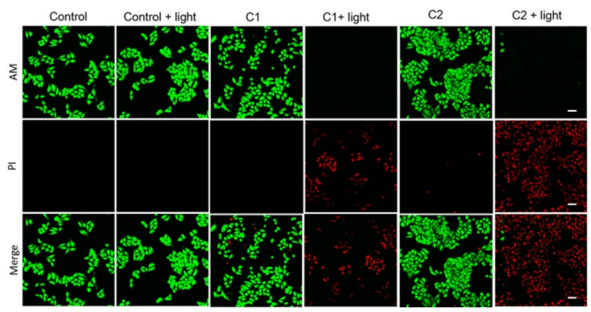

Fig. 6 Calcein-AM and PI labelled cells after PDT treatment. Cells in C1 + light and C2 + light groups were irradiated with 660 nm LED light (18 J cm^{-2}). Scale bars: 20 μm.

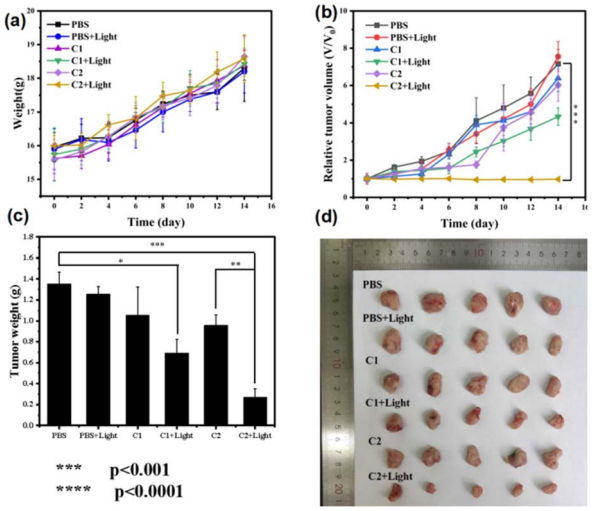

Fig. 7 (a) The weight of the mice changed over the time. (b) The relative tumor volume changed over the time. (c) Tumor weight in each group. (d) Tumor samples in each group.

before treatment and did not grow. These results indicate that C2 has the potential to become a PS for PDT *in vivo*. After 14 days of treatment, mice were dissected and their main organs (heart, liver, spleen, lungs, kidneys, *etc.*) were stained with hematoxylin–eosin (H&E) to study the systemic toxicity of PSs. As shown in Fig. S3, compared with the organs in the PBS group, no abnormalities or pathological changes were found in the organs of the C1 and C2 light groups, indicating that the systemic toxicity of these two PSs was very low.

Experimental

Materials

4-Bromophenylhydrazine hydrochloride (98%), 3-methyl-2-butanone (98%), 4-iodinephenylhydrazine hydrochloride (98%) hexabromohexanoic acid (98%) and general chemicals were purchased from Energy Chemical Co., Bide Pharmatech Ltd and Shanghai Titan Scientific Co., Ltd. Human lung cancer cells (A549), mouse breast cancer cells (4T1) and human liver cancer cells (HepG2) were purchased from Chinese Academy of Sciences Cell Bank. 2,7-Dichlorofluorescein diacetate (DCFH-DA) Detection Kit, Lyso Tracker Red, Mito Tracker Green, Hoechst 33342, calcein AM/propidium iodide (PI) detection kit and JC-1 Detection Kit were purchased from Beyotime Biotechnology Co. (Shanghai). Singlet Oxygen Sensor Green® (SOSG) and dihydrorhodamine 123 (DHR123) were purchased from KeyGen Biotech Co. (Nanjing).

Synthesis of C1 and C2

Preparation of compound 1

5-Bromo-2,3,3-trimethyl-3H-indole. 4-Bromophenylhydrazine hydrochloride (10 mmol, 2.23 g) was dissolved in glacial acetic acid (20 mL). To this solution, 3-methyl-2-butanone (30 mmol, 2.52 g) was added and stirred thoroughly. The resulting solution was heated to 110 °C and refluxed for 5 hours. Next, the reaction

mixture was washed with water, extracted with ethyl acetate. The solvent was then removed to yield a reddish brown viscous liquid, which was the desired product. The yield is 83%. HRMS: $[M + H]^+$:238.02314, found: 238.02292, ^{1}H NMR (400 MHz, DMSO-D_6) δ (ppm): 7.90 (s, 1H), 7.59 (d, J = 8 Hz, 1H), 7.51 (d, J = 8 Hz, 1H), 2.46 (s, 3H), 1.39 (s, 6H); ^{13}C NMR (400 MHz, DMSO-D_6) δ (ppm): 147.40, 131.44, 131.20, 129.35, 126.47, 120.30, 120.05, 54.62, 22.41, 15.57.

5-Iodine-2,3,3-trimethyl-3H-indole. Similarly, replacing 4-bromophenylhydrazine hydrochloride with 4-iodinephenylhydrazine hydrochloride can produce 5-iodine-2,3,3-trimethyl-3*H*-indole. The yield was 82%. HRMS: $[M + H]^+$: 286.00927, found: 286.00748. ^{1}H NMR (400 MHz, DMSO-D_6) δ (ppm): 8.42 (s, 1H), 8.20 (d, J = 8 Hz, 1H), 7.85 (d, J = 8 Hz, 1H), 2.81 (s, 3H), 1.83 (s, 6H); ^{13}C NMR (400 MHz, DMSO-D_6) δ (ppm): 189.55, 172.47, 148.98, 136.69, 131.23, 121.74, 54.22, 22.65, 21.53, 15.43.

Preparation of compound 2. Compound **1** (10 mmol) and hexabromohexanoic acid were added in a reaction flask, followed by the addition of 5 mL of *o*-dichlorobenzene. The mixture was stirred thoroughly and heated to 130 °C for 12 hours. Stop heating and let the reaction mixture cool naturally to room temperature, then large amount of ether was added. The mixture was filtered to obtain a black precipitate. This product can be directly used in the next reaction step without further purification.

Preparation of condensing agent 3. 2,3-dibromo-4-oxobut-2-enoic acid (10 mmol, 2.6 g) was dissolved in anhydrous ethanol (20 mL)to prepare solution A. Aniline (22 mmol, 2.05 g) was dissolved in anhydrous ethanol (10 mL) to prepare solution B. Solution B was slowly added to solution A, then the reaction mixture was heated to 40 °C for 1 hour. After the mixture was allowed to cool to room temperature, approximately 60 mL of ether was then added while stirring vigorously. After some time, a large amount of precipitation was formed. The precipitate was recrystallized from ethanol to yield yellow needle-shaped crystals with a yield of 82%.

HRMS: $[M + H]^+$: 301.03404, found: 301.03253. ^{1}H NMR (400 MHz, DMSO-D_6) δ (ppm): 9.39 (s, 2H), 7.65 (d, J = 8 Hz, 4H), 7.52 (t, J = 8 Hz, 4H), 7.35 (t, J = 8 Hz, 2H), 3.89 (s, 1H); ^{13}C NMR (400 MHz, DMSO-D_6) δ (ppm): 158.13, 139.11, 130.25, 127.52, 120.04, 89.67.

Preparation of cyanine dyes. To the reaction vessel, added 2 equivalents of compound **2**, 1 equivalent of a condensation agent, and 2 equivalents of sodium acetate. Added appropriate amount of acetic anhydride to dissolve the mixture, then heated while stirring at 110 °C for 1 hour. Next, filter the mixture to remove sodium acetate, and evaporate the filtrate to remove the solvent. The crude product was then purified by column chromatography (dichloromethane : methanol = 50 : 1). The yield is 33%.

C1: HRMS: $[M]^+$: 821.0810, found: 821.0803, ^{1}H NMR (400 MHz, DMSO-D_6) δ (ppm): 8.54 (d, J = 13.2 Hz, 2H), 8.02 (s, 2H), 7.62 (d, J = 8 Hz, 2H), 7.50 (d, J = 8 Hz, 2H), 6.32 (d, J = 13.2 Hz, 2H), 4.16 (t, 4H), 2.24 (t, J = 8 Hz, 4H), 1.71 (s, 16H), 1.56 (m, 4H), 1.38 (m, 4H); ^{13}C NMR (400 MHz, DMSO-D_6) δ (ppm): 174.12, 149.82, 143.78, 141.12, 131.29, 125.99, 118.06, 116.45, 113.71, 102.58, 49.66, 47.95, 43.94, 33.73, 26.45, 25.64, 24.21.

C2: HRMS: $[M]^+$: 913.05738, found: 913.05328; ^{1}H NMR (400 MHz, DMSO-D_6) δ (ppm): 8.52 (d, J = 13.6 Hz, 2H), 8.04 (s, 2H), 7.64 (d, J = 8.8 Hz, 2H), 7.51 (d, J = 8.8 Hz, 2H), 6.33 (d, J = 13.6 Hz, 2H), 4.16 (m, 4H), 2.21 (t, J = 8 Hz, 4H), 1.73 (s, 16H), 1.57 (m, 4H), 1.38 (m, 4H).

^{13}C NMR (400 MHz, DMSO-D_6) δ (ppm): 174.15, 149.82, 143.77, 141.13, 131.29, 125.98, 118.07, 116.38, 113.73, 102.58, 49.67, 47.97, 44.01, 33.50, 26.45, 25.67, 24.13.

Detection of $^1O_2$

1,3-Diphenylisobenzofuran (DPBF) undergoes degradation in the presence of $^1O_2$, leading to a decrease in its UV-visible absorption. This property of DPBF can be used to detect the concentration of $^1O_2$. To perform the assay, dissolve a specific concentration of DPBF and probe molecules in the solvent, and then irradiate the mixture with 660 nm light at 30 mW cm^{-2} for a set period. Monitor the changes in UV absorption to study the $^1O_2$ generation. The singlet oxygen quantum yield (Φ_Δ) was calculated using following equation.[32]

$$\Phi_{\Delta\mathrm{sam}} = \Phi_{\Delta\mathrm{std}}\left(\frac{m_{\mathrm{sam}}}{m_{\mathrm{std}}}\right)\left(\frac{F_{\mathrm{std}}}{F_{\mathrm{sam}}}\right)$$

where "sam" and "std" represent the "PSs" and "ICG", respectively. "m" is the slope of absorbance change curve of DPBF at 415 nm, $F = 1–10^{-\mathrm{O.D}}$ (O.D. is the absorbance of the solution at 660 nm).

According to literature methods, SOSG was also used to detect the concentration of $^1O_2$.[35,36] In brief, mix a certain amount of methanol solution of SOSG (Beyotime Biotechnology, Shanghai) with an aqueous solution of PS C1 or C2, so that the concentration of SOSG in the mixture was 5 μM and the concentration of C1 or C2 was 10 μM. Then the mixture was irradiated with 660 nm light (30 mW cm^{-2}). Use a fluorescence spectrometer to record the fluorescence intensity (500–600 nm) every 20 seconds (excitation wavelength: 480 nm).

Detection of $O_2^{\cdot-}$

Similar to the method of detecting $^1O_2$. DHR123 was used to detect the concentration of $O_2^{\cdot-}$. Mix a certain amount of DHR123 with an aqueous solution of PS C1 or C2, so that the concentration of DHR123 in the mixture was 60 μM and the concentration of C1 or C2 was 10 μM. Then the mixture was irradiated with 660 nm light (30 mW cm^{-2}). Use a fluorescence spectrometer to record the fluorescence intensity (500–600 nm) every 20 seconds (excitation wavelength: 480 nm).

Detection of intracellular ROS

HepG2 cells were exposed to specific concentration of C1 and C2 for 4 hours, followed by washing thrice with PBS. Next, the cells were incubated with DCFH-DA probe for 30 minutes, followed by irradiation with 660 nm light 25 mW cm^{-2} for 10 minutes. And the resulting green fluorescence intensity in the cancer cells was visualized using a laser confocal microscope. DCF: λ_{ex} = 488 nm, λ_{em} = 480–520 nm.

Detection of mitochondrial membrane potential

The mitochondrial membrane potential compound was assessed using 5,5′,6,6′-tetrachloro-1,1′,3,3′-tetraethylbenzimidazolocarbocyanine iodide (JC-1) as a probe. A549 cells were incubated in 35 mm confocal dishes for 12 hours at 37 °C in a 5% CO_2 environment. Subsequently, the medium was replaced by fresh medium containing varying concentrations of C1 and C2, and the cells were further incubated for 12 hours. Post-treatment, the cells were stained with JC-1 apoptosis detection kit. Changes in mitochondrial membrane potential were visualized using confocal microscopy. The excitation wavelengths were set at 488 nm and 561 nm, with emission wavelengths collected from 510–550 nm (green channel) and 570–620 nm (red channel).

Subcellular organelle localization

To stain and visualize specific cellular organelles, Lyso Tracker Red, Mito Tracker Green, and Hoechst 33342 dyes were employed to label lysosomes, mitochondria, and nuclei, respectively. The staining solutions were prepared according to the product instructions. Initially, the staining solutions were treated the cells for 30 minutes, followed by washing off the staining solution and the fresh culture medium was added. The cells were then examined using a laser confocal microscope. Lyso Tracker Red: λ_{ex} = 561 nm, λ_{em} = 570–620 nm, Mito Tracker Green:λ_{ex} = 488 nm, λ_{em} = 510–550 nm, Hoechst 33342: λ_{ex} = 405 nm, λ_{em} = 430–470 nm, C1 and C2: λ_{ex} = 660 nm, λ_{em} = 680–720 nm.

In vitro cytotoxicity assay

The *in vitro* cytotoxicity of compounds C1 and C2 was evaluated in 4T1 cells and HepG2 cells using an MTT assay. The specific experimental process can refer to our previous work.[37,38]

Construction of 4T1 mouse tumor model

All animal procedures were in accordance with the Guide for the Care and Use of Laboratory Animal Resources and the National Research Council, and approved by the Institutional Animal Care and Use Committee of Shandong Second Medical University (approval ethics number: 2023SDL238). Six-week-old Balb/C mice were purchased from Beijing Vital River Laboratory Animal Technology Co., Ltd. For *in vivo* evaluation of PDT efficacy of C1 and C2, the mice were randomly divided into six groups (n = 5 mice per group): group 1: PBS injection only; group 2: PBS injection followed by irradiation; group 3: C1 injection only; group 4: C1 injection followed by irradiation; group 5: C2 injection only; group 6: C2 injection followed by irradiation.

Injections of PBS (200 μL) or PSs (200 μL, 1 mg kg^{-1}) were administered intravenously to the mice in each respective group before irradiation. One hour post-injection, the tumor region was exposed with 660 nm light at a power density of 25 mW cm^{-2} for 20 min. Tumor volume was measured every two days over a 14 day period using a vernier caliper. The tumor volume was calculated using the following formula, based on the longest (length) and shortest (width) diameters:

$$V = \frac{a \times b^2}{2}$$

where V represents the tumor volume, a is the long diameter and b is the short diameter.

In vivo biosafety assay

To assess *in vivo* biosafety, mouse weight and histological analysis *via* hematoxylin–eosin (H&E) staining were performed. On the 14th day of treatment, all mice were sacrificed and the tumor tissues were collected. The major organs, including heart, liver, spleen, lung, kidneys were collected for histological examination using H&E staining.

Conclusions

In summary, we have designed and synthesized two pentamethine cyanine dyes as PSs. Both PSs target mitochondria and their maximum absorption wavelengths are in the near-infrared region. ROS experiments have found that PS C1 and C2 not only produced $^1O_2$, but also $O_2^{\bullet -}$. In addition, PS C2 generated a large amount of intracellular ROS after being excited by red light, thereby killing tumor cells. Theoretical calculations have found that C2 can effectively reduce singlet–triplet energy difference (ΔE_{S-T}), which make it easier to intersystem cross (ISC) from excited singlet state to triplet state, thereby increasing the yield of ROS. Animal experiments have shown that C2 could effectively inhibit tumor growth without damaging normal tissues. This study provided a basis for designing I/II type photosensitizers based on cyanine dyes.

Conflicts of interest

There are no conflicts to declare.

Data availability

The data supporting this study's findings are available from the corresponding author upon reasonable request, and some of the data are made available in the SI file.

The SI includes additional characterization data supporting the main findings, such as the synthesis route of compounds C1 and C2, the absorption and fluorescence spectra of photosensitizers C1 (a) and C2 (b), Cellular activity of HepG2 cells subjected to C1 and C2 treatment with and without light. (25 mW, 20 min), main organs (heart, liver, spleen, lungs, kidneys) and tumor were stained with hematoxylin eosin, HRMS and NMR spectra of C1, C2, and intermediates. See DOI: **https://doi.org/10.1039/d5ra05267j**.

Acknowledgements

We are grateful for the grants from the Shandong Provincial Natural Science Foundation of China (ZR2022QB241), Shandong Province Higher Education Undergraduate Teaching Reform Research Project (M2023099).

The authors acknowledge the financial support through the Researchers Supporting Project number (RSP2025R147), King Saud University, Riyadh, Saudi Arabia.

Notes and references

1 H. Sung, J. Ferlay, R. L. Siegel, M. Laversanne, I. Soerjomataram, A. Jemal and F. Bray, *Ca-Cancer J. Clin.*, 2021, **71**(3), 209–249.
2 S. Cao, X. Li, Y. Gao, F. Li, K. Li, X. Cao, Y. Dai, L. Mao, S. Wang and X. Tai, *Dalton Trans.*, 2020, **49**, 11851–11858.
3 S. Kwiatkowski, B. Knap, D. Przystupski, J. Saczko, E. Kedzierska, K. Knap-Czop, J. Kotlinska, O. Michel, K. Kotowski and J. Kulbacka, *Biomed. Pharmacother.*, 2018, **106**, 1098–1107.
4 S. Cao, J. Fan, W. Sun, F. Li, K. Li, X. Tai and X. Peng, *Chem. Commun.*, 2019, **55**, 12956–12959.
5 A. A. AboAlhasan, M. A. S. Sakr, M. F. Abdelbar, H. S. El-Sheshtawy, S. A. El-Daly, E. M. Ebeid, R. H. Al-Ashwal and S. M. Al-Hazmy, *J. Saudi Chem. Soc.*, 2022, **26**(4), 101491.
6 S. Cao, F. Li, Q. Xu, M. Yao, S. Wang, Y. Zhou, X. Cui, R. Man, K. Li and X. Tai, *J. Saudi Chem. Soc.*, 2021, **25**, 101372.
7 S. Tong, Y. Cheng, H. Liu, Y. Pang, X. Lin, Z. Hu and F. Wu, *J. Photochem. Photobiol., A*, 2025, **459**, 116085.
8 J. Xie, Y. Wang, W. Choi, P. Jangili, Y. Ge, Y. Xu, J. Kang, L. Liu, B. Zhang, Z. Xie, J. He, N. Xie, G. Nie, H. Zhang and J. Kim, *Chem. Soc. Rev.*, 2021, **50**(16), 9152–9201.
9 M. Yang, T. Yang and C. Mao, *Angew. Chem., Int. Ed.*, 2019, **58**(40), 14066–14080.
10 W. Chen, Z. Wang, M. Tian, G. Hong, Y. Wu, M. Sui, M. Chen, J. An, F. Song and X. Peng, *J. Am. Chem. Soc.*, 2023, **145**, 8130–8140.
11 X. Hu, Z. Fang, F. Sun, C. Zhu, M. Jia, X. Miao, L. Huang, W. Hu, Q. Fan, Z. Yang and W. Huang, *Angew. Chem., Int. Ed.*, 2024, **63**(15), e202401036.
12 S. Tang, G. Li, H. Zhang, Y. Bao, X. Wu, R. Yan, Z. Wang and Y. Jin, *Biomater. Sci.*, 2023, **11**(9), 3128–3143.
13 X. Fan, S. Lv, F. Lv, E. Feng, D. Liu, P. Zhou and F. Song, *Chem.–Eur. J.*, 2024, **30**, e202304113.
14 D. Liu, H. An, X. Li, B. Wang, S. Zhao, M. Lan, Z. Yang and X. Song, *Luminescence*, 2024, **39**, e70028.
15 Y. Xiao, Y. Yuan, M. Liang, J. Ni, L. Yu, Z. Huang, B. Du and Y. Quan, *Dyes Pigm.*, 2023, **220**, 111765.
16 J. Shi, M. Liang, Y. Qiu, J. Zhang, S. Wang, H. Fang, Y. Jiang, X. Ye, Y. Luo, Z. Huang and Y. Quan, *Talanta*, 2025, **282**, 127074.
17 J. Yuan, H. Yang, W. Huang, S. Liu, H. Zhang, X. Zhang and X. Peng, *Chem. Soc. Rev.*, 2025, **54**, 341.
18 K. Kang, Y. Wu, X. Zhang, S. Wang, S. Ni, J. Shao, Y. Du, Y. Yu, Y. Shen, Y. Chen and W. Chen, *Eur. J. Med. Chem.*, 2025, **286**, 117306.
19 W. Song, H. Yang, Y. Wang, S. Chen, W. Zhong, Q. Wang, W. Ding, G. Xu, C. Meng, Y. Liang, Z. Chen, S. Cao, L. Wei and F. Li, *Adv. Sci.*, 2024, **11**(30), 2307765.
20 C. C. Cankaranlk, G. Karanlk and A. Erdomu, *Appl. Organomet. Chem.*, 2025, **39**(6), e70184.
21 W. Porolnik, N. Karpinska, M. Murias, J. Piskorz and M. Kucinska, *Biomedicines*, 2025, **13**(2), 297.
22 Q. Wang, F. Li, H. Yang, Y. Wang, W. Ding, F. Dai, L. Wei, S. Cao and W. Song, *Chem. Commun.*, 2022, **58**, 8536–8540.
23 L. Peng, W. Chen, H. Hou, M. Tian, F. Song, W. Zheng and X. Peng, *Dyes Pigm.*, 2023, **217**, 111426.
24 L. Yang, Q. Chen, Y. Wan, S. Gan, S. Li, C. Lee, Y. Jiang, H. Zhang and H. Sun, *Chem. Commun.*, 2022, **58**, 9425–9428.
25 Y. Gu, H. Lai, Z. Chen, Y. Zhu, Z. Sun, X. Lai, H. Wang, Z. Wei, L. Chen, L. Huang, Y. Zhang, F. He and L. Tian, *Angew. Chem., Int. Ed.*, 2023, **62**, e202303476.
26 K. Wen, H. Tan, Q. Peng, H. Chen, H. Ma, L. Wang, A. Peng, Q. Shi, X. Cai and H. Huang, *Adv. Mater.*, 2022, **34**, 2108146.
27 S. Banfi, E. Caruso, S. Caprioli, L. Mazzagatti, G. Canti, R. Ravizza, M. Gariboldi and E. Monti, *Bioorg. Med. Chem.*, 2004, **12**, 4853–4860.
28 G. Jori, *J. Photochem. Photobiol., B*, 1996, **36**(2), 87–93.
29 Y. Sun, X. Jiang, Z. Liu, L. Liu, Y. Liao, L. Zeng, Y. Ye and H. Liu, *Eur. J. Med. Chem.*, 2020, **208**, 112794.
30 L. Yang, P. Gao, Y. Huang, X. Lu, Q. Chang, W. Pan, N. Li and B. Tang, *Chin. Chem. Lett.*, 2019, **30**(6), 1293–1296.
31 S. Yan, L. Dong, Z. Hu, Y. Zhang, W. Xu, J. H. Xing and J. Zhang, *Molecules*, 2023, **28**(15), 5874.
32 X. Zhao, Q. Yao, S. Long, W. Chi, Y. Yang, D. Tan, X. Liu, H. Huang, W. Sun, J. Du, J. Fan and X. Peng, *J. Am. Chem. Soc.*, 2021, **143**, 12345–12354.
33 X. Hao, Y. Tang, R. Zhang, Z. Wang, M. Gao, R. Wei, Y. Zhao, X. Mu, Y. Lu and X. Zhou, *Acta Biomater.*, 2024, **178**, 287–295.
34 J. Lu, J. Ding, Z. Xia, Z. Yang, C. Lv, S. Zong, J. Cao, D. Zhou, S. Long, W. Sun, J. Du, J. Fan and X. Peng, *J. Am. Chem. Soc.*, 2025, **147**, 18100–18109.
35 J. Liu, H. Chen, Y. Yang, Q. Wang, S. Zhang, B. Zhao, Z. Li, G. Yang and G. Deng, *Mater. Horiz.*, 2023, **10**, 3791–3796.
36 H. Chen, S. Yan, L. Zhang, B. Zhao, C. Zhu, G. Deng and J. Liu, *Sens. Actuators, B*, 2024, **405**, 135346.
37 S. Cao, A. Wang, K. Li, Z. Lin, H. Yang, X. Zhang, J. Qiu and X. Tai, *RSC Adv.*, 2023, **13**, 26324–26329.
38 S. Cao, X. Tai, K. Li, A. Zhang, P. Ma, G. Sui, L. Zhang, X. Tian, A. Wang and M. Azam, *J. Mol. Struct.*, 2025, **1325**, 141040.